First Results From The Hertzsprung Song Telescope

Grundahl, F.; Andersen, M. Fredslund; Christensen-Dalsgaard, J.; Antoci, V.; Kjeldsen, H.; Handberg, R.; Houdek, G.; Bedding, T. R.; Pallé, P. L.; Jessen-Hansen, J.; Aguirre, V. Silva; White, T. R.; Frandsen, S.; Albrecht, S.; Andersen, M. I.; Arentoft, T.; Brogaard, K.; Chaplin, W. J.; Harpsøe, K.; Jørgensen, U. G.

Document Version
Publisher's PDF, also known as Version of record

Link to publication on Research at Birmingham portal

First Results from the Hertzsprung SONG Telescope: Asteroseismology of the G5 Subgiant Star μ Herculis[*]

F. Grundahl[1], M. Fredslund Andersen[1], J. Christensen-Dalsgaard[1], V. Antoci[1], H. Kjeldsen[1], R. Handberg[1], G. Houdek[1], T. R. Bedding[1,2], P. L. Pallé[3,4], J. Jessen-Hansen[1], V. Silva Aguirre[1], T. R. White[1], S. Frandsen[1], S. Albrecht[1], M. I. Andersen[5], T. Arentoft[1], K. Brogaard[1], W. J. Chaplin[1,6], K. Harpsøe[7], U. G. Jørgensen[7], I. Karovicova[8], C. Karoff[1,9], P. Kjærgaard Rasmussen[5], M. N. Lund[1,6], M. Sloth Lundkvist[1,10], J. Skottfelt[7,11], A. Norup Sørensen[5], R. Tronsgaard[1], and E. Weiss[1]

[1] Stellar Astrophysics Centre (SAC), Department of Physics and Astronomy, Aarhus University, Ny Munkegade 120, DK-8000 Aarhus, Denmark; fgj@phys.au.dk
[2] Sydney Institute for Astronomy, School of Physics, University of Sydney 2006, Australia
[3] Instituto de Astrofísica de Canarias, E-38205 La Laguna, Tenerife, Spain
[4] Universidad de La Laguna, Dpto. Astrofsica, E-38206 La Laguna, Tenerife, Spain
[5] Niels Bohr Institute, University of Copenhagen, Juliane Maries vej 30, DK-2100 Copenhagen, Denmark
[6] School of Physics and Astronomy, University of Birmingham, Edgbaston, Birmingham B15 2TT, UK
[7] Niels Bohr Institute and Centre for Star and Planet Formation, University of Copenhagen, Øster Voldgade 5, DK-1350 Copenhagen K, Denmark
[8] Zentrum für Astronomie der Universität Heidelberg (ZAH), Institut für Theoretische Astrophysik, Albert-Ueberle-Str. 2, D-69120 Heidelberg, Germany
[9] Department of Geoscience, Aarhus University, Høegh-Guldbergs Gade 2, DK-8000 Aarhus C, Denmark
[10] Zentrum für Astronomie der Universität Heidelberg, Landessternwarte, Königstuhl 12, D-69117 Heidelberg, Germany
[11] Centre for Electronic Imaging, The Open University, Milton Keynes MK7 6AA, UK

Abstract

We report the first asteroseismic results obtained with the Hertzsprung Stellar Observations Network Group Telescope from an extensive high-precision radial-velocity observing campaign of the subgiant μ Herculis. The data set was collected during 215 nights in 2014 and 2015. We detected a total of 49 oscillation modes with l values from zero to three, including some $l = 1$ mixed modes. Based on the rotational splitting observed in $l = 1$ modes, we determine a rotational period of 52 days and a stellar inclination angle of 63°. The parameters obtained through modeling of the observed oscillation frequencies agree very well with independent observations and imply a stellar mass between 1.11 and 1.15 $M_\odot$ and an age of $7.8^{+0.3}_{-0.4}$ Gyr. Furthermore, the high-quality data allowed us to determine the acoustic depths of the He II ionization layer and the base of the convection zone.

Key words: asteroseismology – instrumentation: spectrographs – methods: data analysis – methods: observational – stars: individual (HD 161797) – stars: oscillations

1. Introduction

Asteroseismology of solar-like oscillations has blossomed as an observational science in the past few years, thanks to the steady flow of high-precision photometry from the *CoRoT* and *Kepler* space missions (see Chaplin & Miglio 2013, for a review). From *Kepler*, we now have oscillation spectra, based on four years of continuous observations, for hundreds of main-sequence stars and tens of thousands of red giants. However, ground-based spectroscopic measurements of solar-like oscillations (see Bedding 2012 and references therein for a review) still have an important role to play. They can be used to target specific stars of interest anywhere in the sky, and they can provide a higher signal-to-noise ratio than photometry because the stellar background from granulation is much lower in velocity than intensity compared to the oscillations (see, e.g., Grundahl et al. 2007, Figure 1). This property makes the detection of lower frequency and $l = 3$ modes less difficult. Subgiants are particularly interesting for asteroseismology because some of their oscillations occur as mixed modes, which have characteristics of both pressure and gravity modes and are very sensitive to the conditions in the stellar core (Christensen-Dalsgaard et al. 1995).

SONG (Stellar Observations Network Group) is planned as a network of 1 m telescopes that will carry out high-precision radial-velocity measurements of stars. The first node at Observatorio del Teide on Tenerife has been operating since 2014 and consists of the Hertzsprung SONG Telescope, which is equipped with a coudé échelle spectrograph with an iodine cell (Grundahl et al. 2007). Here, we present observations over two observing seasons (2014 and 2015) of the G5 subgiant star μ Herculis (μ Her). Importantly, this star turns out to have a frequency spacing that is highly favorable for single-site observations (Arentoft et al. 2014). Our observations span a total of 215 nights and have yielded an oscillation spectrum with a high signal-to-noise ratio and a high frequency resolution, allowing the most detailed asteroseismic study ever performed for a subgiant observed from the ground.

2. Basic Properties of μ Her

The star μ Her (HD 161797, HR 6623, HIP 86974) is a bright G5 subgiant. Solar-like oscillations were detected by Bonanno et al. (2008) using iodine-referenced radial-velocity observations over seven nights with the 3.6 m Italian TNG Telescope on La Palma. They detected a clear excess of power centered at a frequency of $\nu_{\rm max} = 1200$ μHz and found the most likely value for the large frequency separation to be $\Delta\nu = 56.5$ μHz. Based on this value, Bonanno et al. (2008) extracted frequencies for 15 individual oscillation modes, which were subsequently used for theoretical modeling (Pinheiro & Fernandes 2010; Yang & Meng 2010).

Table 1
Classical Parameters for μ Her

Parameter	Value	Uncertainty	Reference
$T_{\rm eff}$ [K]	5560	80	J15, our uncertainty
[Fe/H] [dex]	0.28	0.07	J15, our uncertainty
$\log g$ [dex]	3.98	0.10	J15, our uncertainty
$v \sin i$ [km s^{-1}]	1.7	0.4	J15
Parallax [mas]	120.33	0.16	van Leeuwen (2007)
$\theta_{\rm LD}$[mas]	1.93	0.03	Derived here
$R/R_\odot$	1.73	0.02	Derived here
$L/L_\odot$	2.54	0.08	Derived here
M_V	3.82	0.03	Derived here
System velocity [km s^{-1}]	−17.07	0.12	SIMBAD
$\log R'_{\rm HK}$	−5.1	0.1	Isaacson & Fischer (2010)

In the following sections, we discuss the fundamental stellar properties of μ Her as input for modeling the measured oscillation frequencies. Estimates for the radius and luminosity are also provided for later comparison to the model results.

2.1. T_{eff}, log g, and [Fe/H]

Because of its brightness, the basic parameters for μ Her have been determined in many studies. The most recent publication is the 2016 version of the PASTEL catalog (Soubiran et al. 2016), which also summarizes nearly all literature values.

The reported effective temperature determinations range from 5397[12] to 5650 K, $\log g$ from 3.7 to 4.1 and [Fe/H] values between $+0.04$ and $+0.3$. Most of these studies employed "standard" 1D–LTE analysis of high-resolution, high signal-to-noise spectra to determine these parameters and arrived at slightly different conclusions. We do not have a quantitative way to decide which values are the best. We therefore adopted the most recent parameters (Jofré et al. 2015, hereafter J15) and list them in Table 1. To reflect that this choice is a compromise, we assigned larger uncertainties than reported by J15. Specifically, Bruntt et al. (2010) have discussed the accuracy of the determination of stellar temperature, gravity, and [Fe/H] and concluded that realistic error bars for these quantities are 80 K, 0.08 dex, and 0.07 dex, respectively. We have adopted these values here. Finally, J15 also determined $v \sin i = 1.7$ km s^{-1}, which is in accordance with expectations for an old, slightly evolved low-mass star.

2.2. Luminosity and Radius

To estimate the luminosity, we used the measured $V = 3.42$ (Bessell 2000), the *Hipparcos* parallax (120.33 ± 0.16 mas), and assumed $A_V = 0$, which yielded $M_V = 3.82$. The bolometric correction was calculated using Equation (9) from Torres (2010). We used the Casagrande & VandenBerg (2014) V filter bolometric corrections and found $-0^{\rm m}086$ and $-0^{\rm m}068$ for μ Her and the Sun, respectively. Based on these values, we determined $L = 2.54 \pm 0.08\,L_\odot$.

The radius can be determined from angular-diameter measurements. Observations of μ Her were recently made with the Precision Astronomical Visual Observations beam combiner (Ireland et al. 2008) at the Center for High Angular Resolution Astronomy Array (ten Brummelaar et al. 2005). A fit of a uniform-disk model to these observations resulted in a uniform-disk diameter of $\theta_{\rm UD} = 1.821 \pm 0.018$ mas (I. Karovicova et al. 2017, in preparation). We determined a linear limb-darkening coefficient in the R band (0.60 ± 0.04) by interpolating the model grids of Claret & Bloemen (2011) to the spectroscopic values of $T_{\rm eff}$, $\log g$, and [Fe/H]. The subsequent limb-darkened diameter is determined to be $\theta_{\rm LD} = 1.93 \pm 0.02$ mas. Using the parallax, this translates to a radius of $R = 1.73 \pm 0.02\,R_\odot$.

While angular diameters are often used to determine effective stellar temperatures, we have opted not to do this here because we have found three independent literature values for the bolometric flux that differ by 25%, which makes it problematic to select the correct value (Mozurkewich et al. 2003; Boyajian et al. 2013; Baines et al. 2014). We note that if we adopt the luminosity from photometry, our interferometric radius and neglecting the uncertainty in the parallax, the inferred temperature for μ Her becomes 5540 ± 80 K, which is fully consistent with the adopted spectroscopic temperature.

2.3. Activity

There are only two reports on the activity level for μ Her, based on the Ca HK lines: Wright et al. (2004) reported $\log R_{\rm HK} = -5.11$ and Isaacson & Fischer (2010) found $\log R_{\rm HK} = -5.08$. Both values are lower than the level found for the Sun, suggesting that μ Her is a rather inactive star, consistent with its evolutionary stage. This is, however, contradicted by the newly released measurements by the Mount Wilson Observatory HK Project.[13] These measurements of μ Her indicate an abrupt change in the S index from 0.14 to more than 0.3. At this stage, it is impossible to conclude whether this jump is of stellar origin, and only additional data can solve this ambiguity.

2.4. Multiplicity

Roberts et al. (2016) provided a detailed summary of the quadruple nature of μ Her. All other components of the system are M-type dwarfs. Interestingly, the inner pair (μ Her and one of the M-dwarfs) of the system has an orbital inclination of $63° \pm 5°$ (Roberts et al. 2016), which agrees very well with the inclination of the μ Her rotation axis determined from our seismic measurements (see Section 7). From the analysis of published radial-velocity and astrometric measurements, Roberts et al. (2016) determined an orbital period of ~ 100 years and concluded that this pair is currently close to the lower inflection point of the radial-velocity curve. We expect to cover this portion of the orbit with SONG radial-velocity measurements in the coming years.

3. The SONG Prototype and Observations of μ Her

μ Her was observed with the automated 1 m Hertzsprung SONG telescope (Andersen et al. 2014) at Observatorio del Teide during the summers of 2014 (105 nights) and 2015 (110 nights). All spectra for radial-velocity determination were collected through an iodine cell for precise wavelength

---

[12] Baines et al. (2014) provided a $T_{\rm eff}$ estimate of 5317 K based on an angular-diameter measurement. The low value $T_{\rm eff}$ is probably due to a low value for the estimated bolometric flux, with a reported uncertainty, which appears to be unrealistically small. Note also that the reported parallaxes for μ Her and HD 188512 in their Table 2 are incorrect.
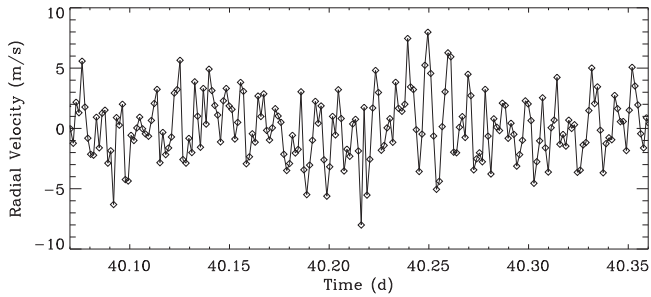
[13] http://www.nso.edu/node/1335

Figure 1. Seven hours of raw μ Her velocity data for one of the best nights in 2014. The high quality of the data allows us to directly see the oscillations in the time-series data.

Figure 2. Times series for μ Her after 4σ clipping for the observations from 2014 (top) and 2015 (bottom panel).

calibration. Each observation consisted of a 120 s exposure, with 2.3 s readout time for the CCD camera. A spectral resolution of 90,000 was used throughout the entire observing campaign. The median count per pixel at 5560 Å was 25514 ADU. The spectra have 51 spectral orders covering 4400–6900 Å. A total of nearly 30,000 spectra were collected during the two observing seasons. All the 2014 spectra were reduced using an IDL-based pipeline that uses the routines of Piskunov & Valenti (2002). For the 2015, data the extraction pipeline was based on the C++ re-implementation of the same routines by Ritter et al. (2014). Before each observing night, calibration frames (bias frames, flat fields, and ThAr spectra) were obtained and applied nightly. The extracted spectra, with the superimposed iodine absorption spectrum, were analyzed with the code iSONG (e.g., Corsaro et al. 2012; Antoci et al. 2013). This code closely follows the procedures outlined by Butler et al. (1996) to extract the stellar radial velocities. To generate the required intrinsic stellar template, the bright fast-rotating star HR 6410 was observed at $R = 110,000$ to determine the spectral-line-spread function of the spectrograph. This was used to deconvolve a high-S/N spectrum of μ Her obtained without the iodine cell. For each spectrum, the RV code extracted velocities in 24 spectral orders, each subdivided into 22 "chunks" of 91 pixels (approximately 2 Å). This resulted in 528 independent radial-velocity estimates. We calculated the final velocities as the weighted average velocity of all chunks. The noise was estimated from the power-spectrum analysis in Section 4, resulting in an average precision of $\sim 1.5\,\mathrm{m\,s^{-1}}$ per spectrum. For each exposure, we calculated the barycentric Julian mid-time and barycentric velocity correction using the program BarCor[14] by M. Hrudková.

4. Initial Processing of the Time Series

The quality of the data is very high (a 7 hr segment from one of the best nights of the time series is shown in Figure 1). However, the data quality does vary slightly from night to night, and also within nights, as a function of zenith distance, seeing, and instrumental effects. In order to optimize the signal-to-noise ratio in the power spectrum, we estimated the statistical quality of each measurement. To do this, we first created a high-pass-filtered version by smoothing the time series with a Gaussian filter with an FWHM of 500 s, which was then subtracted from the original data to remove all p-mode oscillations and long-term drifts. This filtered time series was used to estimate the local variance, σ_i^2, which we calculated as the moving mean of the square over a duration of 6 hr (about 180 data points). In this way, only slow changes were included in the estimates of the
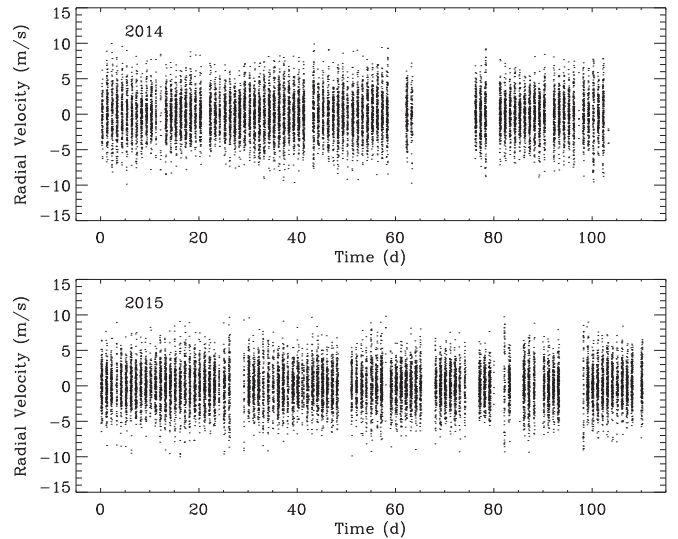
local variance. Data points that deviated more than four times the local root-mean-square (rms) scatter were removed from the raw time series and from the high-pass filtered series. This 4σ clipping removed 3.9% of the data points from the 2014 and 1.4% from the 2015 data sets. This new high-pass filtered time series was then used to recalculate the variances, σ_i^2, and weights were assigned to each data point as

$$w_i = \frac{1}{\sigma_i^2}. \qquad (1)$$

The median rms noise is $1.47\,\mathrm{m\,s^{-1}}$ and the best observing periods have noise levels below $1.3\,\mathrm{m\,s^{-1}}$ (16% of the data points). The noise levels are above $2\,\mathrm{m\,s^{-1}}$ for only 6% of the data points.

After removing the bad data and assigning statistical weights to each data point, we calculated the power spectrum, as described in the next section. The full time series is shown in Figure 2. Note that the nightly average was subtracted from each night, which removes long-period variations but does not affect the oscillation signal.

5. Data Analysis

5.1. Calculating the Power Spectrum

The power spectrum of the μ Her time series was calculated as a weighted fit of sinusoids, following the algorithms described by Frandsen et al. (1995) and Handberg (2013). We calculated power spectra separately for the 2014 and 2015 series, and then combined them into one power spectrum as a weighted average based on their mean noise levels. The relative weights were 42% and 58% for the 2014 and 2015 data, respectively. The individual and combined power spectra are shown in Figure 3.

The noise level in the combined power spectrum corresponds to $2\,\mathrm{cm\,s^{-1}}$ in amplitude at a frequency of $3000\,\mu\mathrm{Hz}$, which translates to $19.4\,\mathrm{cm^2\,s^{-2}\,\mu Hz^{-1}}$ in power density. This is similar to the noise levels in the α Cen A and B time series data (see Bedding et al. 2004; Butler et al. 2004; Kjeldsen et al. 2005). For example, the noise level in amplitude for α Cen B was $1.4\,\mathrm{cm\,s^{-1}}$ at $7000\,\mu\mathrm{Hz}$, but close to $2\,\mathrm{cm\,s^{-1}}$ at $3000\,\mu\mathrm{Hz}$. Thus the 1 m
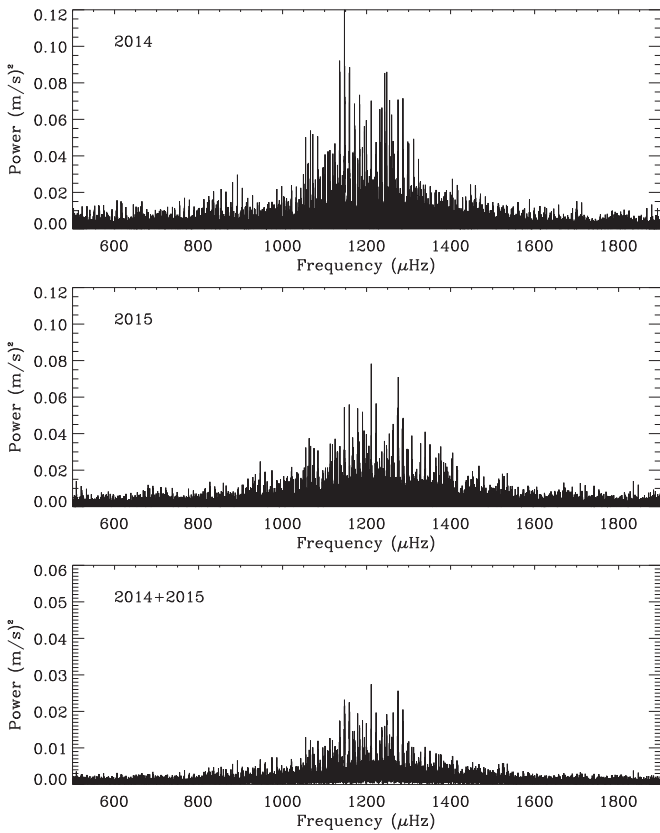
---

[14] sirrah.troja.mff.cuni.cz/~mary

Figure 3. Power spectra for the individual series from 2014 and 2015 data as well as the combined spectrum. For details see the text.

Figure 4. Spectral windows for the 2014 and 2015 data.

SONG telescope and spectrograph has achieved a noise level in μ Her over the 200 nights that is comparable to that achieved with the 8 m VLT and 4 m AAT over nine nights in a star that is seven times brighter.

Extraction of mode frequencies was done in the combined power spectrum. A large number of p-modes are clearly present, especially near the maximum power at 1200 μHz. However, the single-site data result in a complicated spectral window with strong sidelobes. The spectral windows for the 2014 and 2015 data are shown in Figures 4 and 5.

5.2. Identifying the p-modes

As a next step, we determined the large frequency separation. Figure 6 shows the autocorrelation of the power spectrum after smoothing with a Gaussian of FWHM 0.5 μHz, for frequency shifts between 0 and 100 μHz. The peaks at 11.6 and 23.1 μHz correspond to 1 and 2 cycles per day, respectively, arising from the daily gaps. We can identify the large frequency separation of μ Her as $\Delta\nu = 64$ μHz. This value for $\Delta\nu$ agrees with the prediction by Bedding et al. (1996), which was based on their estimates of the mass and radius of the star. It is also consistent with the observed value of $\nu_{\max} = 1200$ μHz. Our measurement disagrees with the value of 56.5 μHz determined by Bonanno et al. (2008) based on seven nights of radial-velocity measurements. However, we note that in their Figure 3, which is a comb-response function of their power spectrum (analogous to an autocorrelation), there is a secondary peak close to 64 μHz. The incorrect determination of $\Delta\nu$ is most likely due to the short time span of the observations and the confusion with the daily sidebands.
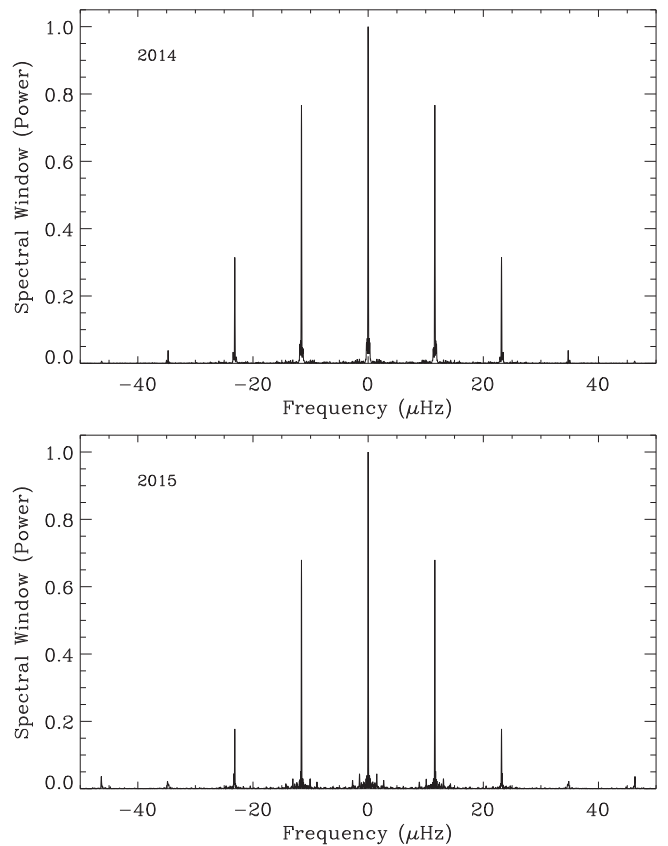
Figure 7 illustrates the observed power spectrum in échelle format, where we see clear vertical ridges corresponding to modes with different degrees. We tested other values of $\Delta\nu$ and found that none gave the same clear structure of vertical ridges. Due to the single-site nature of the data, the first and second daily sidelobes are prominent. To locate the individual oscillation modes, we constructed a folded power spectrum using the following procedure. We first smoothed the power spectrum by using a Gaussian function with a FWHM of 1 μHz. This was then folded with a spacing of 64 μHz between 976 μHz and 1424 μHz (7 radial orders, centered at 1200 μHz). The resulting folded power spectrum is shown in Figure 8, where the positions of modes of different degrees ($l = 0$, 1 and 2) can be seen. We used the peaks identified in Figure 8 to estimate the parameters in the asymptotic relation (Tassoul 1980; Scherrer et al. 1983; Christensen-Dalsgaard 1988):

$$\nu(n, l) \approx \Delta\nu\left(n + \tfrac{1}{2}l + \epsilon\right) - l(l + 1)D_0. \tag{2}$$

We found $\Delta\nu = 64.2$ μHz, $D_0 = 0.80$ μHz, and $\epsilon = 1.44$. Note that this value of ϵ is consistent with expectations for a star with the effective temperature of μ Her (White et al. 2012).

Using Equation (2), we estimated the expected frequencies of the individual p-modes and identified them in the power spectrum. Thanks to the high data quality, we also detected five $l = 3$ modes in the range of 1100–1400 μHz, where the S/N is highest. Additionally, one bumped $l = 1$ mixed mode is apparently present at low frequencies.

In total, we identified 49 probable modes, shown as filled symbols in the right panel of Figure 7, superimposed on a smoothed version of the observed power spectrum. The open
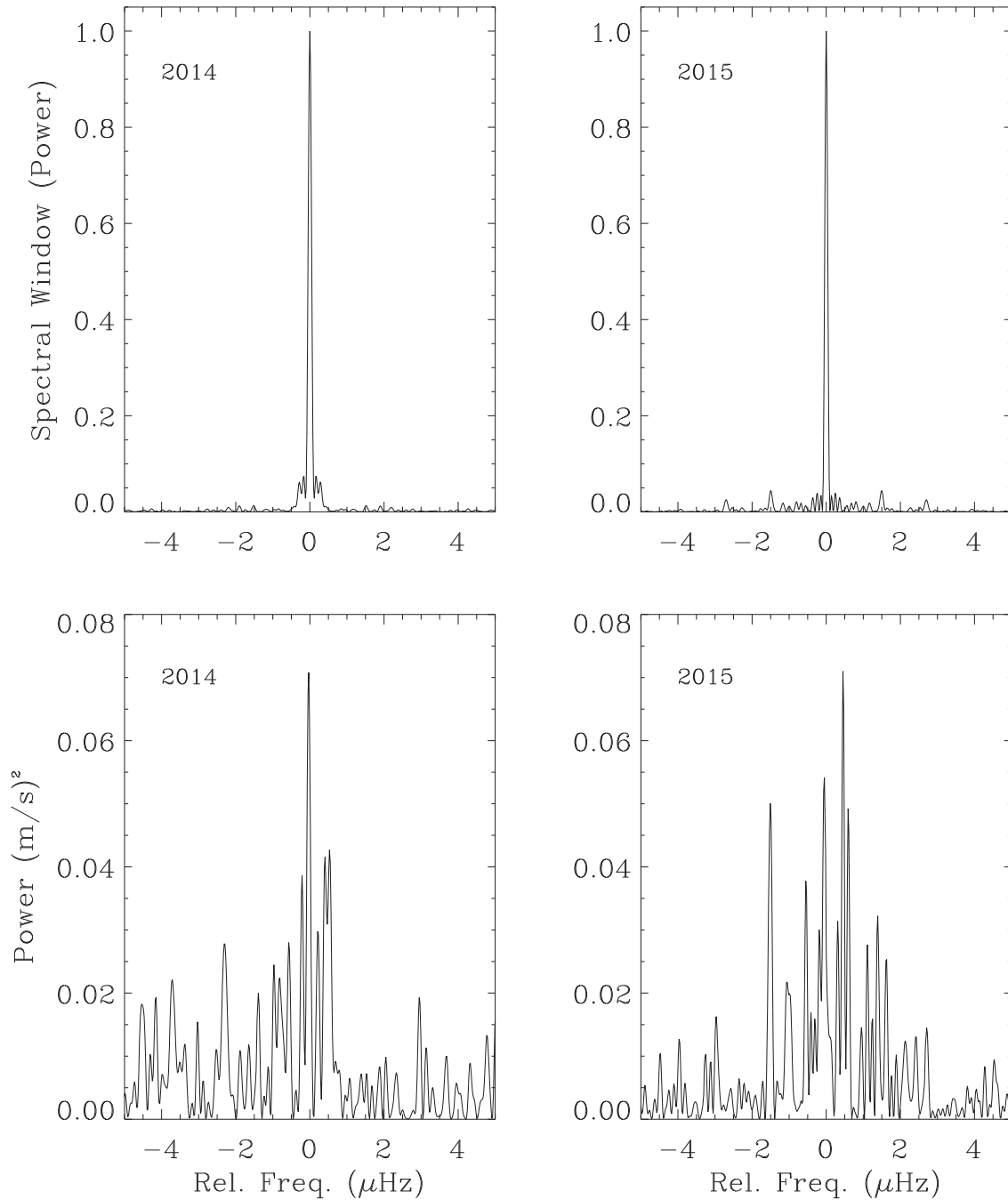
Figure 5. Upper panels: close-ups of the spectral windows for the 2014 and 2015 data. Lower panels: close-up view of the frequency peak at 1274.93 μHz showing the spread of oscillation power caused by the stocastic nature of the oscillations.

symbols show the first and second daily sidelobes on either side of each mode. It is remarkable that none of the sidelobes coincide with other p-modes or their sidelobes. It is extremely fortunate that the single-site spectral window has little impact on our efforts to identify and measure the oscillation modes. Indeed, it seems that its frequency spacings make μ Her an ideal target for single-site observations (see Arentoft et al. 2014, for a discussion of SONG's spectral window and its influence on choice of targets).

We estimated uncertainties in the frequencies based on their S/N using a procedure similar to Kjeldsen et al. (2005, Section 4). These frequencies and their uncertainties were used as input for the Markov Chain Monte-Carlo (MCMC) frequency

extraction described in Section 5.4. The identified modes in the central part of the spectrum, together with their daily sidelobes, are shown in Figure 9.

5.3. Amplitude and Frequency of Maximum Power

To determine the frequency of maximum power (ν_{max}) and the peak oscillation amplitude (A_{osc}) for μ Her, we followed the procedure described in Section 3.2 of Kjeldsen et al. (2008). This involves smoothing the power spectrum to estimate the total power in the oscillations in a manner that is insensitive to the spectral window.

We found the following values: $\nu_{max} = 1216 \pm 11$ μHz and $A_{osc} = 38.9 \pm 1.2$ cm s^{-1}. Note that this velocity amplitude
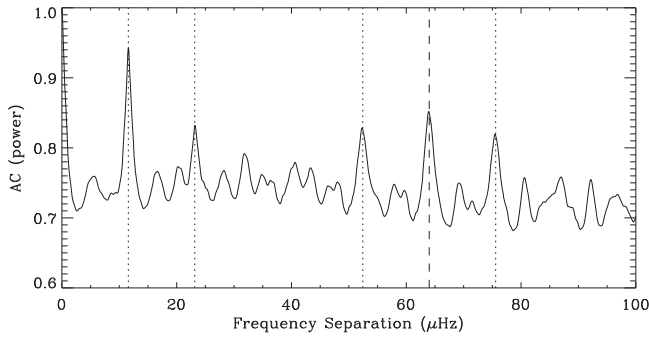
Figure 6. Autocorrelation of the power spectrum smoothed using a Gaussian with a FWHM of 0.5 μHz. The dashed line indicates the peak at 64 μHz that we identify as the large separation, together with extra peaks (dotted lines) corresponding to daily sidelobes in the spectral window.

corresponds to radial modes and is 2.08 ± 0.10 times the mean solar value (see Kjeldsen et al. 2008 for details).

Interestingly, the oscillation amplitude for μ Her decreased significantly from 2014 to 2015. This is clearly seen in Figure 3. Analyzing the two power spectra separately, as described above, showed the peak amplitude to be 41.6 ± 1.7 cm s^{-1} in 2014 and 36.1 ± 1.5 cm s^{-1} in 2015.

5.4. Extraction of Mode Properties Using MCMC Analysis

The next step was to measure parameters for the 49 individual modes using an MCMC analysis. In order to use the full time span of the measurements we constructed a full time series using all the available data from the two observing runs. The two time series were concatenated, but the gap between them was reduced to 80 days. This can be justified by the fact that we are searching for stochastic oscillations where the mode lifetime is significantly shorter than 80 days. In this way we ensure that any oscillations from the 2014 data set will have disappeared and do not affect the 2015 data set. This concatenation creates a better window function. The final power density spectrum and corresponding spectral window function were then calculated from the time series specified above, following the prescriptions outlined in Section 4.

5.4.1. MCMC Peakbagging

The fit to the power spectrum was performed using the APT MCMC algorithm (Handberg & Campante 2011) and the preliminary frequencies determined in Section 5.2 were used as starting guesses. We ran four million iterations, which were subsequently thinned to two million, using 10 parallel tempering levels to avoid local maxima solutions. The model limit spectrum that was fitted to the observed power spectrum was defined as

$$\mathcal{P}(\nu) = \eta(\nu) \sum_{n,l} \sum_{m=-l}^{l} \frac{H_{nl} \mathcal{E}_{lm}(i)}{1 + \frac{4}{\Gamma_{nl}^2}(\nu - \nu_{nl} - m\delta\nu_s)^2} + N(\nu) \tag{3}$$

where ν_{nl} is the mode frequency, H_{nl} is the mode height, Γ_{nl} is the linewidth (which is inversely proportional to the mode lifetime), and $\delta\nu_s$ is the rotational splitting. The factor $\eta(\nu) \equiv \mathrm{sinc}^2(\Delta T_{int}\nu)$ is the attenuation of signals arising from the non-zero integration time (ΔT_{int}). The noise model $N(\nu)$ was simply a white-noise profile across the region of interest.

In order to limit the number of free parameters, H_{nl} and Γ_{nl} were linearly interpolated in frequency between H_{n0} and Γ_{n0}, respectively, and the height was scaled with the visibility of the mode (see Handberg & Campante 2011). The relative heights of rotationally split components within a multiplet were taken as (Gizon & Solanki 2003)

$$\mathcal{E}_{lm}(i) = \frac{(l - |m|)!}{(l + |m|)!} \{P_l^{|m|}(\cos i)\}^2 \tag{4}$$

where $P_l^m(x)$ are the associated Legendre functions.

Instead of using the mode height, H_{nl}, directly as the free parameter in the fit, the mode amplitude was used. This is less correlated with the linewidth, Γ_{nl}, and therefore provides a more stable fit. The conversion from amplitude to height was done following Fletcher et al. (2006), which allows for linewidths becoming comparable to the frequency resolution. Similarly, the projected rotational splitting, $\nu_s \sin i$, was used as the free parameter instead of the rotational splitting itself, to avoid known correlations.

Uniform priors were set for mode frequencies, the rotational splitting and the inclination angle, whereas modified Jeffreys priors were used for mode heights and linewidths.

In order to account for the single-site window function, the model spectrum, $P(\nu)$, was convolved with the spectral window in each iteration of the MCMC. This has a very significant impact on the computing time, but is essential in order to describe the spread of power to sidelobes due to the non-continuous observations.

From the resulting Markov chain, the final parameters and errors listed in Table 2 were estimated from the full posterior probability distributions as the median values and 68.3% confidence interval. The final mode frequencies (with uncertainties) were corrected for the systemic radial-velocity Doppler shift ($v_{rad} = -17.07 \pm 0.12$ km s^{-1}) in order to list the frequencies in the rest frame of the star (Davies et al. 2014).

Finally, we calculated the frequency-separation ratio as defined by Roxburgh & Vorontsov (2003), which are used in the following sections for modeling of the observations:

$$r_{01}(n) = \frac{1}{8} \frac{\nu_{n-1,0} - 4\nu_{n-1,1} + 6\nu_{n,0} - 4\nu_{n,1} + \nu_{n+1,0}}{\nu_{n,1} - \nu_{n-1,1}} \tag{5}$$

$$r_{02}(n) = \frac{\nu_{n,0} - \nu_{n-1,2}}{\nu_{n,1} - \nu_{n-1,1}} \tag{6}$$

$$r_{10}(n) = \frac{-1}{8} \frac{\nu_{n-1,1} - 4\nu_{n,0} + 6\nu_{n,1} - 4\nu_{n+1,0} + \nu_{n+1,1}}{\nu_{n+1,0} - \nu_{n,0}}. \tag{7}$$

These were calculated using the full Markov chains for each frequency coming from the MCMC analysis, yielding the full correlation matrices between all ratios.

From the MCMC analysis, we were also able to constrain the rotational splitting between the different m-components of the $l = 1$ multiplets. We also measured the stellar inclination angle, based on the relative heights of these m-components (Gizon & Solanki 2003; see Figures 10 and 11). The resulting rotational period is $P_{rot} = 52^{+3}_{-1}$ days and the stellar rotational inclination angle is $i = 63^{+9}_{-10}$ degrees. Both values and their errors were determined as the mode values and 68.3% confidence intervals in Figures 10 and 11.
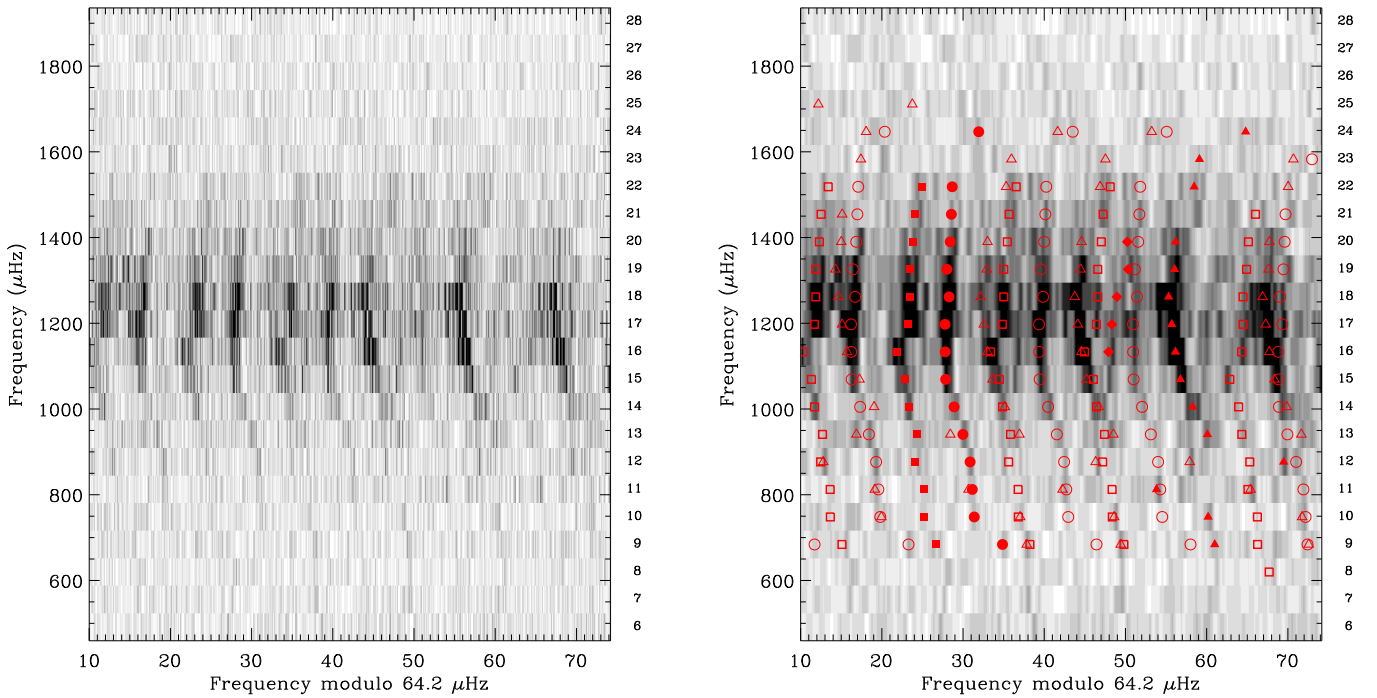
Figure 7. Observed power spectrum of μ Her in échelle format as a grayscale image, with no smoothing (left) and smoothed to a resolution of 0.5 μHz (right). In the right plot, the filled symbols show the 49 possible modes that we have identified (see the text). The open symbols show the first and second daily sidelobes on each side of these modes. Symbol type indicates the mode degree: $l=0$ (circles), $l=1$ (triangles), $l=2$ (squares), and $l=3$ (diamonds). The numbers on the right of each plot show the radial order, which corresponds to n for the $l=0$ modes.

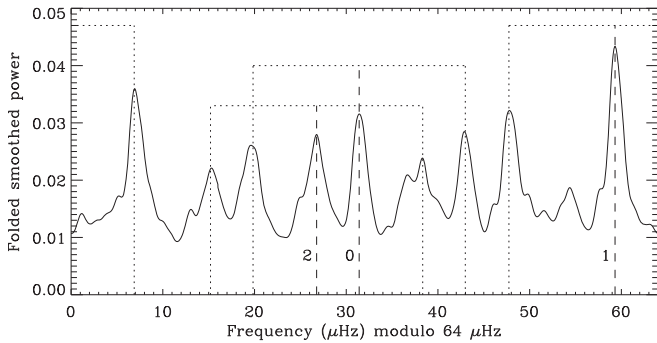**Figure 8.** Folded smoothed power spectrum for the frequency range of 976–1424 μHz. The peaks correspond to $l=0$, 1, and 2 shown by long dashed lines as well as the spectral window (1/d) shown by dotted lines.
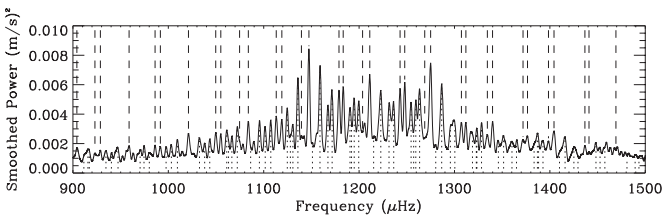

Figure 9. Central part of the combined power spectrum for μ Her, smoothed with a Gaussian having a FWHM of 3 μHz to enhance the visibility of the peaks. Dashed lines above the smoothed power spectrum show the peaks identified to be oscillation modes; the dotted lines below illustrate their daily sidelobes.

6. Modeling the Oscillations

Once the oscillation frequencies were extracted, we used different codes and procedures to model the observations of μ Her. In this section, we provide detailed descriptions of this endeavor.

Table 2
Frequencies (μHz) for Individual Oscillation Modes Extracted from the MCMC Analysis, Listed in échelle Format (see Figure 7)

n	$l=2$	$l=0$	$l=3$	$l=1$
24	$1636.68^{+0.30}_{-0.45}$	$\cdots$	$\cdots$	$1669.55^{+0.27}_{-0.37}$
23	$\cdots$	$\cdots$	$\cdots$	$1599.67^{+0.68}_{-0.22}$
22	$1501.34^{+0.20}_{-0.42}$	$1505.04^{+0.21}_{-0.72}$	$\cdots$	$1534.83^{+0.72}_{-0.30}$
21	$1436.28^{+0.05}_{-0.10}$	$1440.74^{+0.02}_{-0.05}$	$\cdots$	$\cdots$
20	$1371.87^{+0.24}_{-0.33}$	$1376.41^{+0.10}_{-0.14}$	$1398.21^{+0.53}_{-0.43}$	$1404.15^{+0.12}_{-0.17}$
19	$1307.24^{+0.13}_{-0.12}$	$1311.81^{+0.08}_{-0.13}$	$1334.13^{+0.52}_{-0.25}$	$1339.85^{+0.10}_{-0.10}$
18	$1243.05^{+0.07}_{-0.06}$	$1247.89^{+0.04}_{-0.04}$	$1268.56^{+0.11}_{-0.27}$	$1274.93^{+0.05}_{-0.06}$
17	$1178.69^{+0.11}_{-0.09}$	$1183.20^{+0.05}_{-0.05}$	$1203.74^{+0.37}_{-0.26}$	$1211.12^{+0.05}_{-0.06}$
16	$1113.04^{+0.05}_{-0.07}$	$1119.03^{+0.06}_{-0.07}$	$1139.15^{+0.57}_{-0.18}$	$1147.38^{+0.04}_{-0.04}$
15	$1049.94^{+0.21}_{-0.11}$	$1054.90^{+0.06}_{-0.06}$	$\cdots$	$1083.81^{+0.06}_{-0.06}$
14	$986.14^{+0.12}_{-0.09}$	$991.75^{+0.11}_{-0.14}$	$\cdots$	$1021.14^{+0.13}_{-0.15}$
13	$922.93^{+0.08}_{-0.12}$	$928.64^{+0.06}_{-0.06}$	$\cdots$	$958.75^{+0.17}_{-0.17}$
12	$858.51^{+0.13}_{-0.04}$	$865.34^{+0.10}_{-0.12}$	$\cdots$	$903.95^{+0.08}_{-0.07}$
11	$795.49^{+0.02}_{-0.45}$	$801.42^{+0.06}_{-0.49}$	$\cdots$	$824.11^{+0.26}_{-0.03}$
10	$731.32^{+0.15}_{-0.15}$	$737.47^{+0.27}_{-0.21}$	$\cdots$	$766.27^{+0.03}_{-0.02}$
9	$668.56^{+0.19}_{-0.05}$	$676.76^{+0.02}_{-0.03}$	$\cdots$	$702.89^{+0.08}_{-0.08}$

Note. Note that n corresponds to the radial order for the $l=0$ modes.

6.1. Fits to Individual Frequencies

We fitted the 49 frequencies in Table 2 and their ratios following procedures described by Silva Aguirre et al. (2015), in this case taking into account the presence of the mixed modes. One fit was applied to the individual frequencies, which were assumed to be statistically independent. A grid of models and oscillation frequencies was calculated using the ASTEC stellar evolution code (Christensen-Dalsgaard 2008a) and the
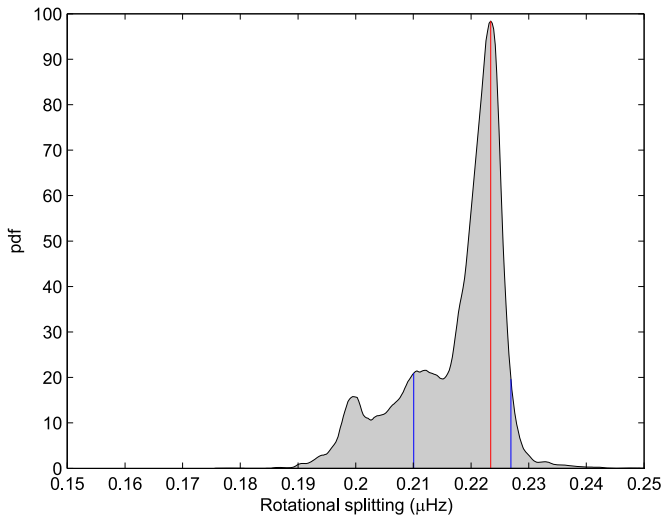
Figure 10. Probability density function (pdf) for the rotational frequency splitting from MCMC analysis. The red vertical line indicates the mode of the posterior distribution, and the two blue vertical lines show the 68.3% highest probability density region.

Figure 11. Probability density function (pdf) for the inclination angle of μ Her from MCMC analysis. The red vertical line indicates the mode of the posterior distribution, and the two blue vertical lines show the 68.3% highest probability density region.
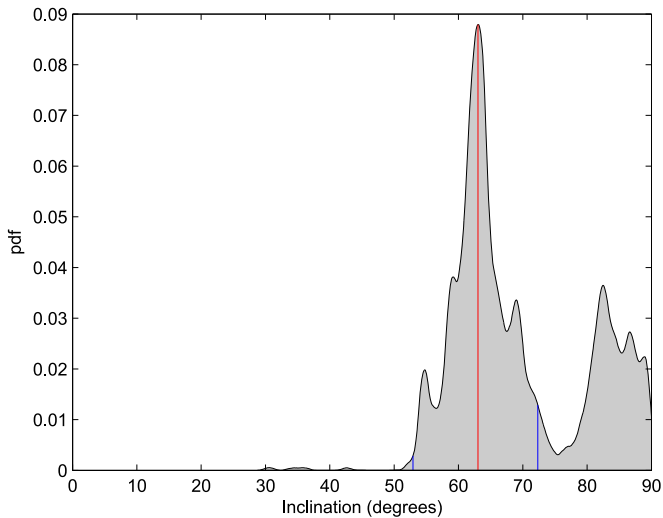
ADIPLS adiabatic pulsation code (Christensen-Dalsgaard 2008b). The evolution modeling used the OPAL equation of state (Rogers & Nayfonov 2002) and OPAL opacities (Iglesias & Rogers 1996), supplemented by the Ferguson et al. (2005) low-temperature opacities. The nuclear reaction rates were obtained from the NACRE compilation (Angulo et al. 1999). Diffusion and settling of helium and heavy elements were not included. Convection was described using the mixing-length formalism (Böhm-Vitense 1958), and convective overshoot was not included. The grid spanned a large range in mass and composition, though was constrained by an assumed Galactic chemical evolution model with $\Delta Y / \Delta Z = 1.4$, where Y and Z are the abundances of helium and heavy elements, respectively. Models with three values of the mixing-length parameter α_{ML}, 1.5, 1.8, and 2.1, were included, where $\alpha_{\mathrm{ML}} = 1.8$ roughly corresponds to the solar calibration.

To match the observed frequencies, the computed frequencies were corrected for the errors introduced by the treatment of the near-surface layers by applying a fitted scaled solar surface correction (Christensen-Dalsgaard 2012), described in more detail, together with other aspects of this so-called ASTFIT fitting technique, by Silva Aguirre et al. (2015). Briefly, the fit is carried out by minimizing, along each evolution sequence,

$$\chi^2 = \chi^2_{\mathrm{spec}} + \chi^2_{\nu}. \tag{8}$$

Here, χ^2_{spec} is based on observed values of T_{eff} and [Fe/H] (see Table 1), and

$$\chi^2_{\nu} = \frac{1}{N-1} \sum_{i=1}^{N} \left(\frac{\nu_i^{(\mathrm{obs})} - \nu_i^{(\mathrm{mod})}}{\sigma_i} \right)^2 \tag{9}$$

is based on the observed frequencies $\nu_i^{(\mathrm{obs})}$ and standard deviations σ_i listed in Table 2. The remaining observed properties were not included in the fit but were used to check the results. The model frequencies, $\nu_i^{(\mathrm{mod})}$, included the surface correction (see above). An initial minimization was carried out between timesteps in the evolution sequence by assuming that the frequencies scale as $R^{-3/2}$. This defined a minimum χ^2_{min} for each evolution track in the grid. The best-fitting models were found by locating the smallest resulting values of χ^2_{min}.

Owing to the presence of mixed modes, the $R^{-3/2}$ scaling of the frequencies is not universally valid, leading to potential systematic errors in the fits. To correct for this, the fit was refined by computing, in the vicinity of the minima determined by the above scaling procedure, frequencies for a small set of models suitably interpolated between timesteps in the evolution sequence. As shown by Christensen-Dalsgaard & Houdek (2010), this allows us to fully resolve the behavior of the frequencies in the vicinity of an avoided crossing involving mixed modes. In practice, this was applied only to evolution tracks where the χ^2_{min} as determined by the simple procedure was less than twice the minimum among the values of χ^2_{min} so determined.

The stars analyzed by Silva Aguirre et al. (2015) were all on the main sequence and the observed modes were purely acoustic. In contrast, μ Her is a subgiant with clearly identified mixed modes (Figure 12), and the relevant models also have several mixed modes. This complicates the identification of the observed modes with those of the models in the grid. We have applied a relatively simple technique to identify the relevant model modes in cases with mixed modes, taking into account that the present observations show only one nonradial mode of each degree in each interval between two adjacent radial modes. Thus in each radial-mode interval, we chose (with an exception noted below) the frequency of a given degree that minimized the normalized inertia

$$Q_{nl} = \frac{E_{nl}}{\bar{E}_0(\nu_{nl})}, \tag{10}$$

where E_{nl} is the inertia of the mode and $\bar{E}_0(\nu_{nl})$ is the radial-mode inertia, interpolated logarithmically to the frequency ν_{nl} of the given mode. The underlying assumption is that this is the mode most likely to be observed.

For $l = 2$ and 3, there was typically a clear minimum of Q_{nl} among the relevant modes, and the above procedure produced a reasonable fit. For $l = 1$, however, there may be two modes in a given radial-mode interval with comparable values of Q_{nl}, and there is a risk that the selected mode does not provide the
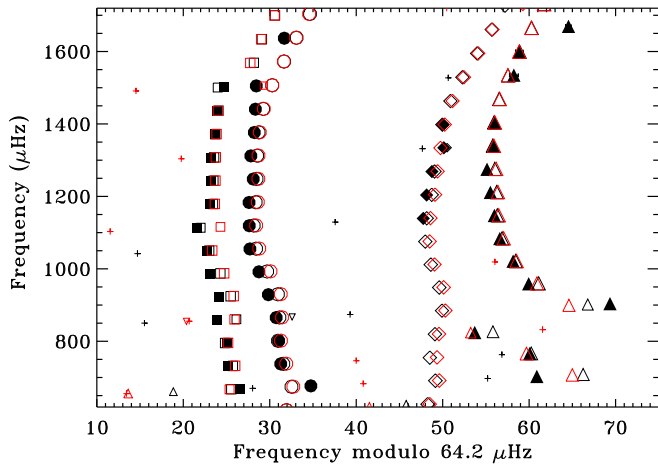
Figure 12. Échelle diagram of observed and fitted frequencies. The filled black symbols show the frequencies provided in Table 2, while the black and red open symbols are for best-fitting models, after solar-scaled surface correction, with masses of, respectively, 1.12 and 1.15 $M_\odot$ (model ASTFIT1 and ASTFIT2 in Table 3). Circles, triangles, squares, and diamonds show results for $l = 0, 1, 2$, and 3, respectively. Symbol sizes are based on a rough estimate of mode amplitudes, relative to the neighboring radial mode (see Christensen-Dalsgaard et al. 1995) For $l = 2$ and 3, small symbols, corresponding to strongly mixed modes, have been replaced by pluses. Inverted triangles at a frequency near $860\,\mu$Hz mark strongly mixed dipolar modes.
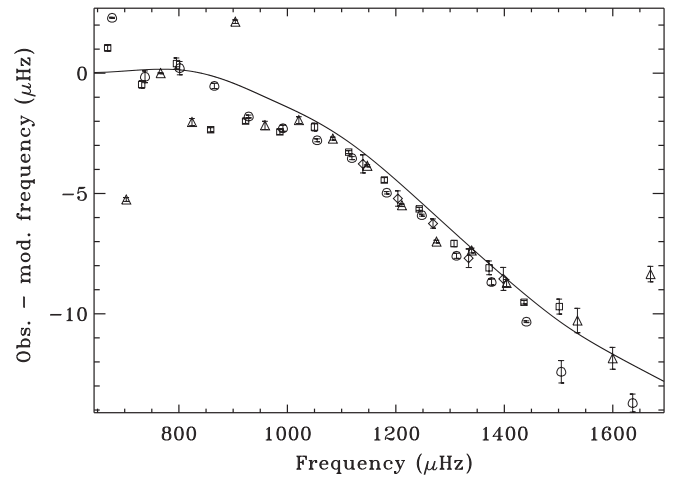

Figure 13. Differences between observed frequencies (Table 2) and model frequencies, without surface correction, for the 1.12 $M_\odot$ model ASTFIT1 in Table 3. The same symbols are used as in Figure 12. The curve shows the scaled solar surface correction used in the fit.

optimal fit to the observations. To circumvent this problem, the procedure was modified by including in the minimization a suitably weighted measure of the distance to the nearest observed dipolar mode. Although fairly crude, this method yielded a reasonable behavior of the fit along the evolution tracks.

As applied by Silva Aguirre et al. (2015), ASTFIT determined likelihood-weighted averages of the various stellar parameters. In the present case, we have found that χ_ν^2 (see Equation (9)) is dominated by a few modes, particularly the dipolar mode undergoing avoided crossing, and hence this statistical procedure has little meaning (see also Figure 13). For this preliminary analysis, we therefore simply considered a few examples of optimized fits for representative selected evolution tracks, chosen to yield values of $T_{\rm eff}$ and [Fe/H] within 2σ of the observed values and χ_ν^2 near its minimum value. These are listed in Table 3. Two examples, with masses of 1.12 $M_\odot$ and 1.15 $M_\odot$, are shown in the échelle diagram in Figure 12. Figure 13 shows the resulting frequency differences for the 1.12 $M_\odot$ model, compared to the fitted surface function.

To determine the uncertainties in the stellar properties, we also fitted combinations of p-mode dominated frequencies using the BAyesian STellar Algorithm (BASTA, see Silva Aguirre et al. 2015). Briefly, this Bayesian approach relies on a large grid of stellar models to determine the probability density function of a given stellar property based on the fit to a set of observational quantities. In this case, we considered the spectroscopic constraints $T_{\rm eff}$ and [Fe/H] and the frequency-separation ratios r_{01} and r_{10} above 1000 μHz (to avoid the impact of the mixed modes in the fit) as the input parameters to be reproduced. We report in Table 3 the median and the 16 and 84 percentiles of the posterior probability density function. The results are in excellent agreement with those obtained with ASTFIT, as well as with the independent radius determination from interferometry.

Using the effective temperature, large frequency separation, and [Fe/H] (see Table 4) as inputs, we also calculated the

stellar parameters using the Asteroseismology Made Easy (AME Lundkvist et al. 2014) grid-based method and found the values to be in agreement with those listed in Table 3.

6.2. Modeling Amplitudes and Mode Lifetimes

Mode linewidths and amplitudes can be used to test models of stellar structure and stability. In particular, comparison between observations and models can be used to calibrate the parameters in the convection model used in the numerical stability analysis. In Figure 14, theoretical estimates of linear damping rates[15] of radial modes are compared to the SONG observations. These computations were performed for global model parameters of the models ASTFIT1 and ASTFIT2 (see Table 3).

The depth of the (surface) convection zone was calibrated to the values obtained from the seismic models ASTFIT1 and ASTFIT2 described in Section 6.1. The basic stability computations were as in Houdek (2006) using Gough's (1977a, 1977b) nonlocal, time-dependent convection model, but adopted for the stellar atmosphere a temperature—optical depth $(T-\tau)$ relation from Trampedach et al. (2014) 3D hydrodynamical simulations. The agreement with the observations is reasonably good.

We also estimated the maximum value of the velocity amplitudes of the acoustic oscillations. Various excitation models have been used in the past to estimate amplitudes of stochastically excited oscillations (Goldreich & Keeley 1977; Balmforth 1992; Samadi & Goupil 2001; Chaplin et al. 2005; Houdek 2006). Here we adapt the scaling relation by Chaplin et al. (2011) for estimating the maximum velocity amplitude. Adopting the global parameters listed in Table 1, we estimate for μ Her a relative maximum velocity amplitude $V/V_\odot \simeq 1.83$ ($V_\odot$ being the maximum solar velocity amplitude), which is in reasonable agreement with the observed value of 2.08 ± 0.10 discussed in Section 5.3. We should, however, note that the β function in Chaplin et al. (2011) Equation (7) is rather uncertain and will add to the uncertainty from the adopted effective temperature for μ Her. The predicted value of the

---
[15] The mode lifetime τ and the linewidths Γ are related through $\tau = 1/\pi\Gamma$.

Table 3
Results of Model Fits

Model	M ($M_\odot$)	R ($R_\odot$)	L ($L_\odot$)	$T_{\rm eff}$ (K)	[Fe/H] (dex)	Age (Gyr)
ASTFIT1	1.12	1.71	2.7	5650	0.26	7.6
ASTFIT2	1.15	1.73	2.6	5600	0.30	7.9
BASTA	$1.11^{+0.01}_{-0.01}$	$1.71^{+0.01}_{-0.02}$	$2.6^{+0.1}_{-0.1}$	5600^{+50}_{-50}	$0.21^{+0.06}_{-0.06}$	$7.8^{+0.3}_{-0.4}$
From Table 1		1.73 ± 0.02	2.54 ± 0.08	5560 ± 80	0.28 ± 0.07	

Table 4
Summary of Results

Parameter	Value	Comment
$T_{\rm eff}$ [K]	5560 ± 80	J15
$\log g$ [cgs]	3.98 ± 10	J15
[Fe/H]	0.28 ± 07	J15
$v \sin i$ [km s^{-1}]	1.7 ± 0.4	J15
$\theta_{\rm LD}$ [mas]	1.93 ± 0.03	measured
R [$R_\odot$]	1.73 ± 0.02	angular diameter + parallax
L [$L_\odot$]	2.54 ± 0.08	assuming $A_V = 0$
$\nu_{\rm max}$ [μHz]	1216 ± 11	measured
$\Delta\nu$ [μHz]	64.2 ± 0.2	measured
ϵ	1.44	measured
i [°]	63^{+9}_{-10}	measured
$P_{\rm rot}$ [day]	52^{+3}_{-1}	measured
age [Gyr]	$7.8^{+0.3}_{-0.4}$	from model
M [$M_\odot$]	1.11 ± 0.01	from model
R [$R_\odot$]	1.72 ± 0.02	from model
L [$L_\odot$]	2.6 ± 0.1	from model
$\log g$ [cgs]	4.01 ± 0.01	from model
$\tau_{\rm II}$ [s]	1938	from model
τ_c [s]	4488	from model

Figure 14. Measured linewidths for radial modes from the MCMC analysis in Section 5.4 (full width at half maximum, symbols) are compared to theoretical estimates of twice the linear damping rates. The black and red curves are the theoretical estimates from nonadiabatic stability analysis adopted for the global parameters of the models ASTFIT1 and ASTFIT2 respectively (see Table 3). Only the mixing-length parameter was modified between the two stability analyses to reproduce the same surface-convection-zone depths as in the two stellar models.

velocity amplitude will therefore capture the uncertainties in both the observations and the scaling relation.

6.3. Using Acoustic Glitches

Abrupt variations in the sound speed, which are called acoustic glitches, produce seismic signatures in the spacing of the observed frequencies. From these seismic signatures, the locations of the abrupt variation (in terms of acoustic depth τ) can be estimated. Figure 15 displays observed second differences $\Delta_2\nu_{n,l} := \nu_{n-1,l} - 2\nu_{n,l} + \nu_{n+1,l}$ of low-degree ($l = 0, 1, 2$, symbols), together with results of the seismic diagnostic D_2 by Houdek & Gough (2007). This analysis adopts Airy functions for the pulsation eigenfunctions and glitches of both stages of helium ionization. We estimated the acoustic depths of the glitches brought about by the second stage of helium ionization, $\tau_{\rm II}$, and by the abrupt variation of the sound speed at the base of the convection zone, τ_c. We found $\tau_{\rm II} \simeq 1938$ s and $\tau_c \simeq 4488$ s. The depths of the acoustic glitches obtained directly from the equilibrium structures of the models listed in Table 3, agree with $\tau_{\rm II}$ to within 3% and for τ_c to within 15%. For the present work, we did not perform an error analysis for the acoustic-glitch depths, but plan to conduct a Monte-Carlo error analysis in an upcoming paper.
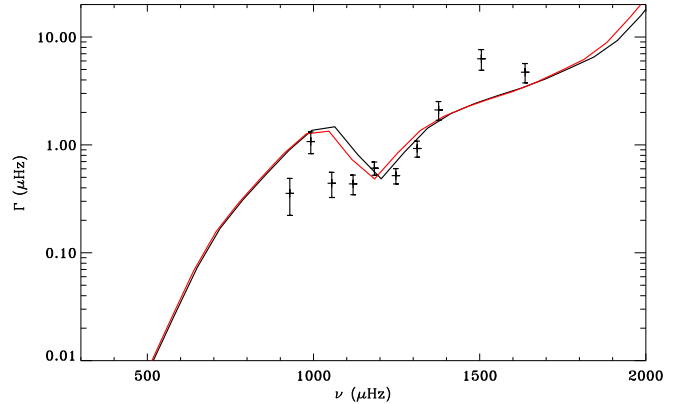
7. Discussion and Outlook

Our 215 nights of observations of μ Her represent the longest ground-based asteroseismology campaign of a solar-like star. For this first SONG long-term target, we have determined all the classical seismic observables and identified 49 oscillation modes (see Table 2). Using MCMC modeling, we measured frequencies and linewidths of radial modes and rotational splitting of $l = 1$ modes. From this, the rotation period and inclination of the rotation axis were determined to be $P_{\rm rot} = 52^{+3}_{-1}$ days and $i = 63^{+9}_{-10}$ degrees (68.3% confidence intervals), respectively. The observed oscillation frequencies were used as input for modeling and, taking into account the detected mixed mode, resulted in accurate determinations of the age as well as radius and luminosity in agreement with the observations (Table 3).

We also compared the observed linewidths with theoretical values and found good agreement at frequencies around and above $\nu_{\rm max}$. For lower frequencies, the mode lifetimes are significantly longer and our data were insufficient to resolve them. With the large number of identified modes and the very good frequency precision, we determined the second frequency differences to measure the acoustic glitches associated with the He II ionization layer and the base of the convection zone. Table 4 provides a full summary of our results.

μ Her is a very interesting seismic target, not only because it is ideal for single-site SONG observations but for several other reasons. For example, μ Her and α Cen A, the best asteroseismically studied bright solar-type stars, have the same mass to
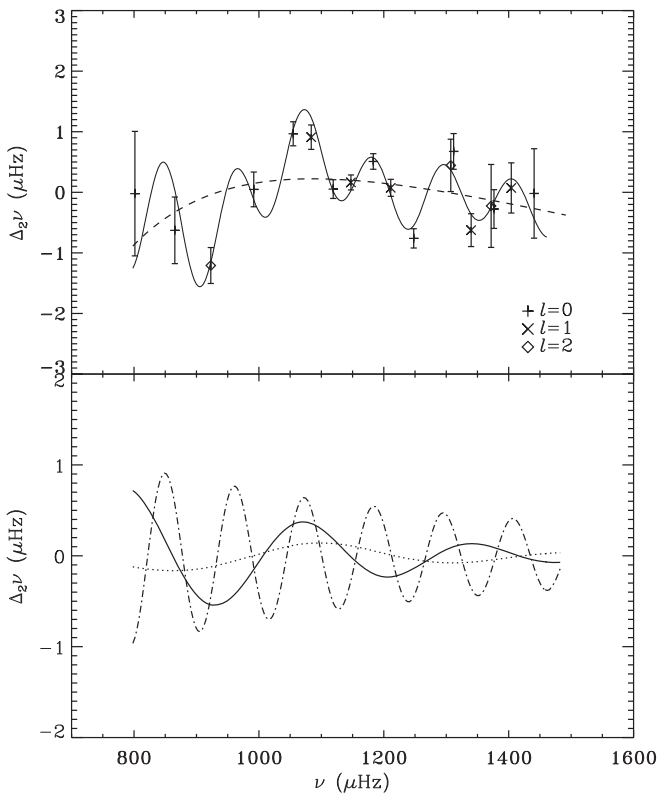
Figure 15. Top: the symbols are second differences $\Delta_2\nu_{n,l} := \nu_{n-1,l} - 2\nu_{n,l} + \nu_{n+1,l}$ of low-degree $(l = 0, 1, 2)$ frequencies obtained from SONG. The vertical bars represent standard errors, evaluated under the assumption that the errors in the raw frequencies are independent. The solid curve is the seismic diagnostic D_2 from Houdek & Gough (2007), determined by fitting by least-squares the seismic diagnostic to $\Delta_2\nu_{n,l}$. The dashed curve represents the smooth contributions from the hydrogen ionization zones and super-adiabatic layer. Bottom: individual contributions of the seismic diagnostic. The solid curve is the contribution of the second stage of helium ionization, the dotted curve displays the first helium ionization contribution and the dotted–dashed curve is the contribution from the base of the convection zone.

within the measurement uncertainties. Very recently Pourbaix & Boffin (2016) redetermined the mass of α Cen A to be $1.133 \pm 0.005\,M_\odot$ as compared to the 1.11–1.15 $M_\odot$ reported here for μ Her. Note that this mass range is where the transition between convective and non-convective core on the main sequence occurs (see Bazot et al. 2016, for an in-depth discussion of α Cen A). Within 0.1 dex, their reported metallicities are also identical. Thus, both stars should be on almost the same evolutionary track, allowing us to undertake comparative studies.

We also note that μ Her (given the metallicity, mass, and age reported here) closely resembles stars in the old open cluster NGC 6791. Thus, differential studies can improve constraints on the helium mass fraction, Y, of μ Her and NGC 6791. If shifted to the reddening and distance of NGC 6791 using the $E(B - V)$ and apparent distance modulus derived by Brogaard et al. (2012), μ Her sits right on the cluster subgiant branch (SGB) of the color–magnitude diagram, confirming the near-identical properties of μ Her and the stars in NGC 6791. The relative spectroscopic $T_{\rm eff}$ of μ Her and SGB twins in the cluster can then be used to tightly constrain the cluster reddening. This can lead to an improved estimate of Y for NGC 6791 through reanalysis of the cluster (Brogaard et al. 2012), which also

allows a precise estimate of Y for μ Her under the assumption of a common helium-to-metal enrichment for stars.

With the results presented here, we are now in the position to learn more about the stellar obliquity[16] of the μ Her system, which is a quadruple system as specified in Section 2.4. From our seismic analysis, we determined the inclination of the stellar rotation axis i of μ Her to be 63^{+9}_{-10} degrees. This is very close to the inclination angle of the orbital plane of μ Her and its closest orbiting component, which is determined to be $63° \pm 5°$ (Roberts et al. 2016).

Combining our measurement of i with the orientation of the orbit does not give us the complete information on the obliquity because we do not know the projection of the stellar spin axis on the plane of the sky. Nevertheless, given the good agreement between the inclination of the stellar rotation axis and the orbital plane, we assume in the following that the rotation axis of μ Her is indeed aligned with the angular momentum of its orbit and briefly discuss this finding. There are only a handful of obliquity measurements in double stars (see Albrecht et al. 2011 for a list) that have a short period (less than one month). Among those, misaligned as well as aligned systems were reported (e.g., Albrecht et al. 2009, 2014, 2007; Triaud et al. 2013). For systems with larger semimajor axes, Hale (1994, and references therein) estimated the stellar inclinations using the projected stellar rotation velocities ($v \sin i$) and found low obliquities in double-star systems with semimajor axes up to $\approx$40 au. However, for systems with more than two stellar components no indication of coplanarity was found. This was interpreted as a sign of long-term secular interactions (Kozai-cycles) between the different components (e.g., Fabrycky & Tremaine 2007; Anderson et al. 2016; Naoz 2016). With an apparently low obliquity for the primary component and a semimajor axis of 2.9 ± 0.3 au, the μ Her system provides an interesting data point that does not seem to follow the trend observed by Hale (1994).

Based on 215 nights of observations we have presented the most detailed study of μ Her to date but there is still much we can learn about this star. We will continue observing μ Her during the coming years to improve the S/N in the power spectrum and the frequency resolution and to check for oscillation amplitude and frequency variations. We expect additional detections of low-frequency modes as well as more $l = 3$ modes, which provide important constraints on the acoustic depth of the He II ionization layer and the convection zone. Longer data sets, and therefore higher S/N, will allow us to detect further mixed modes providing more insights about the deeper regions of the star.

With the upcoming NASA TESS (Transiting Exoplanet Survey Satellite) mission (Ricker et al. 2015), we will be in the position to simultaneously observe μ Her photometrically with TESS and spectroscopically with SONG.[17] This will allow us to measure the oscillation amplitude ratios, providing detailed input on the convective properties of μ Her. The only other solar-type stars where similar observations were performed are the Sun (Jiménez 2002; Houdek 2006) and Procyon (Huber et al. 2011).

---

[16] The angle between the orbital angular momentum and the stellar spin.

[17] μ Her has $R = 2.9$ and $I = 2.5$, which may be too bright for TESS. We note that photometry on strongly saturated stars has been done with success by T. R. White et al. (2017, in preparation) for the *Kepler* mission data; hopefully this will be possible for TESS data as well.

Based on its properties and the unprecedented data set, we expect μ Her to become a benchmark star during the next years. With the addition of more SONG nodes, many of the brightest stars in the sky can be subject to similar comprehensive studies. Such work will provide a reference base of highly accurate parameters for the nearest stars, where the availability of parallaxes and interferometric radii would provide strong model constraints. This will complement future space-based observations from TESS and PLATO.

References

Albrecht, S., Reffert, S., Snellen, I., Quirrenbach, A., & Mitchell, D. S. 2007, A&A, 474, 565
Albrecht, S., Reffert, S., Snellen, I. A. G., & Winn, J. N. 2009, Natur, 461, 373
Albrecht, S., Winn, J. N., Carter, J. A., Snellen, I. A. G., & de Mooij, E. J. W. 2011, ApJ, 726, 68
Albrecht, S., Winn, J. N., Torres, G., et al. 2014, ApJ, 785, 83
Andersen, M. F., Grundahl, F., Christensen-Dalsgaard, J., et al. 2014, RMxAC, 45, 83
Anderson, K. R., Lai, D., & Storch, N. I. 2016, MNRAS, submitted (arXiv:1610.02626)
Angulo, C., Arnould, M., Rayet, M., et al. 1999, NuPhA, 656, 3
Antoci, V., Handler, G., Grundahl, F., et al. 2013, MNRAS, 435, 1563
Arentoft, T., Tingley, B., Christensen-Dalsgaard, J., et al. 2014, MNRAS, 437, 1318
Baines, E. K., Armstrong, J. T., Schmitt, H. R., et al. 2014, ApJ, 781, 90
Balmforth, N. J. 1992, MNRAS, 255, 639
Bazot, M., Christensen-Dalsgaard, J., Gizon, L., & Benomar, O. 2016, MNRAS, 460, 1254
Bedding, T. R. 2012, in ASP Conf. Series 462, Progress in Solar/Stellar Physics with Helio- and Asteroseismology, ed. H. Shibahashi, M. Takata, & A. E. Lynas-Gray (San Francisco, CA: ASP), 195
Bedding, T. R., Kjeldsen, H., Butler, R. P., et al. 2004, ApJ, 614, 380
Bedding, T. R., Kjeldsen, H., Reetz, J., & Barbuy, B. 1996, MNRAS, 280, 1155
Bessell, M. S. 2000, PASP, 112, 961
Böhm-Vitense, E. 1958, ZA, 46, 108
Bonanno, A., Benatti, S., Claudi, R., et al. 2008, ApJ, 676, 1248
Boyajian, T. S., von Braun, K., van Belle, G., et al. 2013, ApJ, 771, 40
Brogaard, K., VandenBerg, D. A., Bruntt, H., et al. 2012, A&A, 543, 106

Bruntt, H., Bedding, T. R., Quirion, P.-O., et al. 2010, MNRAS, 405, 1907
Butler, R. P., Bedding, T. R., Kjeldsen, H., et al. 2004, ApJL, 600, L75
Butler, R. P., Marcy, G. W., Williams, E., et al. 1996, PASP, 108, 500
Casagrande, L., & VandenBerg, D. A. 2014, MNRAS, 444, 392
Chaplin, W. J., Houdek, G., Elsworth, Y., et al. 2005, MNRAS, 360, 858
Chaplin, W. J., Kjeldsen, H., Bedding, T. R., et al. 2011, ApJ, 732, 54
Chaplin, W. J., & Miglio, A. 2013, ARA&A, 51, 353
Christensen-Dalsgaard, J. 1988, in IAU Symp. 123, Advances in Helio- and Asteroseismology, ed. J. Christensen-Dalsgaard & S. Frandsen (Dordrecht: D. Reidel), 295
Christensen-Dalsgaard, J. 2008a, Ap&SS, 316, 13
Christensen-Dalsgaard, J. 2008b, Ap&SS, 316, 113
Christensen-Dalsgaard, J. 2012, AN, 333, 914
Christensen-Dalsgaard, J., Bedding, T. R., & Kjeldsen, H. 1995, ApJ, 443, 29
Christensen-Dalsgaard, J., & Houdek, G. 2010, Ap&SS, 328, 51
Claret, A., & Bloemen, S. 2011, A&A, 529, A75
Corsaro, E., Grundahl, F., Leccia, S., et al. 2012, A&A, 537, A9
Davies, G. R., Handberg, R., Miglio, A., et al. 2014, MNRAS, 445, L94
Fabrycky, D., & Tremaine, S. 2007, ApJ, 669, 1298
Ferguson, J. W., Alexander, D. R., Allard, F., et al. 2005, ApJ, 623, 585
Fletcher, S. T., Chaplin, W. J., Elsworth, Y., Schou, J., & Buzasi, D. 2006, MNRAS, 371, 935
Frandsen, S., Jones, A., Kjeldsen, H., et al. 1995, A&A, 301, 123
Gizon, L., & Solanki, S. K. 2003, ApJ, 589, 1009
Goldreich, P., & Keeley, D. A. 1977, ApJ, 212, 243
Gough, D. O. 1977a, LNP, 71, 15
Gough, D. O. 1977b, ApJ, 214, 196
Grundahl, F., Kjeldsen, H., Christensen-Dalsgaard, J., Arentoft, T., & Frandsen, S. 2007, CoAst, 150, 300
Hale, A. 1994, AJ, 107, 306
Handberg, R. 2013, PhD thesis, Aarhus Univ.
Handberg, R., & Campante, T. L. 2011, A&A, 527, A56
Houdek, G. 2006, ESA SP, 624, 28
Houdek, G., & Gough, D. O. 2007, MNRAS, 375, 861
Huber, D., Bedding, T. R., Arentoft, T., et al. 2011, ApJ, 731, 94
Iglesias, C. A., & Rogers, F. J. 1996, ApJ, 464, 943
Ireland, M. J., Mérand, A., ten Brummelaar, T. A., et al. 2008, Proc. SPIE, 7013, 24
Isaacson, H., & Fischer, D. 2010, ApJ, 725, 875
Jiménez, A. 2002, ApJ, 581, 736
Jofré, E., Petrucci, R., Saffe, C., et al. 2015, A&A, 574, 50
Kjeldsen, H., Bedding, T. R., Arentoft, T., et al. 2008, ApJ, 682, 1370
Kjeldsen, H., Bedding, T. R., Butler, R. P., et al. 2005, ApJ, 635, 1281
Lundkvist, M., Kjeldsen, H., & Silva Aguirre, V. 2014, A&A, 566, 82
Mozurkewich, D., Armstrong, J. T., Hindsley, R. B., et al. 2003, AJ, 126, 2502
Naoz, S. 2016, ARA&A, 54, 441
Pinheiro, F. J. G., & Fernandes, J. M. 2010, Ap&SS, 328, 73
Piskunov, N. E., & Valenti, J. A. 2002, A&A, 385, 1095
Pourbaix, D., & Boffin, H. M. J. 2016, A&A, 586, 90
Ricker, G. R., Winn, J. N., Vanderspek, R., et al. 2015, JATIS, 1, 014003
Ritter, A., Hyde, E. A., & Parker, Q. A. 2014, PASP, 126, 170
Roberts, L. C., Jr., Mason, B. D., Aguilar, J., et al. 2016, AJ, 151, 169
Rogers, F. J., & Nayfonov, A. 2002, ApJ, 576, 1064
Roxburgh, I. W., & Vorontsov, S. V. 2003, A&A, 411, 215
Samadi, R., & Goupil, M.-J. 2001, A&A, 370, 136
Scherrer, P. H., Wilcox, J. M., Christensen-Dalsgaard, J., & Gough, D. O. 1983, SoPh, 82, 75
Silva Aguirre, V., Davies, G. R., Basu, S., et al. 2015, MNRAS, 452, 2127
Soubiran, C., Le Campion, J.-F., Brouillet, N., & Chemin, L. 2016, A&A, 5, A118
Tassoul, M. 1980, ApJS, 43, 469
ten Brummelaar, T. A., McAlister, H. A., Ridgway, S. T., et al. 2005, ApJ, 628, 453
Torres, G. 2010, AJ, 140, 1158
Trampedach, R., Stein, R. F., Christensen-Dalsgaard, J., Nordlund, Å., & Asplund, M. 2014, MNRAS, 442, 805
Triaud, A. H. M. J., Hebb, L., Anderson, D. R., et al. 2013, A&A, 549, 18
van Leeuwen, F. 2007, A&A, 474, 653
White, T. R., Bedding, T. R., Gruberbauer, M., et al. 2012, ApJL, 751, L36
Wright, J. T., Marcy, G. W., Butler, R. P., & Vogt, S. S. 2004, ApJS, 152, 261
Yang, W., & Meng, X. 2010, NewA, 15, 367